Advances in MRI of the myelin bilayer

Weiger, Markus ; Froidevaux, Romain ; Baadsvik, Emily Louise ; Brunner, David Otto ; Rösler, Manuela Barbara ; Pruessmann, Klaas Paul

Abstract: Myelin plays a key role in the function of the central nervous system and is involved in many neurodegenerative diseases. Hence, depiction of myelin is desired for both research and diagnosis. However, MRI of the lipid bilayer constituting the myelin membrane is hampered by extremely rapid signal decay and cannot be accomplished with conventional sequences. Dedicated short-T2 techniques have therefore been employed, yet with extended sequence timings not well matched to the rapid transverse relaxation in the bilayer, which leads to signal loss and blurring. In the present work, capture and encoding of the ultra-short-T2 signals in the myelin bilayer is considerably improved by employing advanced short-T2 methodology and hardware, in particular a high-performance human-sized gradient insert. The approach is applied to tissue samples excised from porcine brain and in vivo in a human volunteer. It is found that the rapidly decaying non-aqueous components in the brain can indeed be depicted with MRI at useful resolution. As a considerable fraction of these signals is related to the myelin bilayer, the presented approach has strong potential to contribute to myelin research and diagnosis.

DOI: https://doi.org/10.1016/j.neuroimage.2020.116888

NeuroImage 217 (2020) 116888

Contents lists available at ScienceDirect

NeuroImage

journal homepage: www.elsevier.com/locate/neuroimage

Advances in MRI of the myelin bilayer

Markus Weiger [*,1], Romain Froidevaux [1], Emily Louise Baadsvik, David Otto Brunner, Manuela Barbara Rösler, Klaas Paul Pruessmann

Institute for Biomedical Engineering, ETH Zurich and University of Zurich, Zurich, Switzerland

ARTICLE INFO

Keywords:
Myelin lipid bilayer
Proteins
Short T2
Super-Lorentzian
High-performance gradient
HYFI

ABSTRACT

Myelin plays a key role in the function of the central nervous system and is involved in many neurodegenerative diseases. Hence, depiction of myelin is desired for both research and diagnosis. However, MRI of the lipid bilayer constituting the myelin membrane is hampered by extremely rapid signal decay and cannot be accomplished with conventional sequences. Dedicated short-T_2 techniques have therefore been employed, yet with extended sequence timings not well matched to the rapid transverse relaxation in the bilayer, which leads to signal loss and blurring. In the present work, capture and encoding of the ultra-short-T_2 signals in the myelin bilayer is considerably improved by employing advanced short-T_2 methodology and hardware, in particular a high-performance human-sized gradient insert. The approach is applied to tissue samples excised from porcine brain and in vivo in a human volunteer. It is found that the rapidly decaying non-aqueous components in the brain can indeed be depicted with MRI at useful resolution. As a considerable fraction of these signals is related to the myelin bilayer, the presented approach has strong potential to contribute to myelin research and diagnosis.

1. Introduction

Myelin plays a key role in the development and function of the central nervous system (CNS), where it is primarily present in white matter (WM). Because demyelination is involved in many neurodegenerative diseases, such as multiple sclerosis, acute disseminated encephalomyelitis, or progressive multifocal leucoencephalopathy (Popescu and Lucchinetti, 2012; Love, 2006), depiction and quantification of myelin are of great interest for both research and diagnosis.

MRI is a preferred candidate for this task due to its versatile contrast and the use of non-ionizing radiation. However, imaging of the myelin membrane is challenged by the extremely rapid decay of its MR signal (Horch et al., 2011; Ramani et al., 2003). The basic constituents of the myelin membrane are lipids, constituting about 80% of all dry mass, and proteins (Morell et al., 1999). The lipid chains are arranged in bilayers which are wrapped around the axons (Morell et al., 1999). This configuration leads to rapid transverse relaxation of the lipid proton signal with a continuum of T_2 values[2] ranging from a few microseconds up to milliseconds, where the dominating contributions stem from the lower end (Wilhelm et al., 2012) (Fig. 1a). Methylene and methyl groups from different locations in the lipid chains contribute to the MR signal as multiple components, each of which can be described as a "super-exponential" decay corresponding to a "super-Lorentzian" spectral lineshape (Bloom et al., 1977; Lawson and Flautt, 1965; Wennerström, 1973). Cumulating the overall T_2 distribution shows that 75% of the myelin lipid signal exhibits T_2 values below 100 μs (Fig. 1b). The majority of the proteins are embedded in the lipid bilayer and also subject to very rapid relaxation due to motional restriction (Wilhelm et al., 2012; Bloom et al., 1969). Thus both lipids and proteins contribute to the ultra-short-T_2 (uT_2) non-aqueous signal of myelin.

As such short-lived signal cannot be detected with conventional MRI, alternative approaches have been developed that utilise aqueous CNS signal for the depiction of myelin. The techniques are based on either unique T_2 properties of the intra- and extracellular water trapped between the myelin bilayers (MacKay et al., 1994; Laule et al., 2007), magnetisation transfer between non-aqueous protons and water (Varma et al., 2015; Gass et al., 1994), or effects of myelin content on overall relaxation times (Sigalovsky et al., 2006; Glasser and Van Essen, 2011). Despite the considerable progress achieved with these methods, detection of the myelin bilayer itself would be beneficial to get alternative

* Corresponding author. Institute for Biomedical Engineering, ETH Zurich and University of Zurich, Gloriastrasse 35, CH-8092, Zurich, Switzerland.
E-mail address: weiger@biomed.ee.ethz.ch (M. Weiger).

[1] Authors contributed equally to this work.

[2] Note that T_2 and not T_2^* is used to characterise the decay of the non-aqueous myelin signal although none of the two concepts is fully suited for semi-solids. Additional effects of T_2' are negligible at the relevant timescale.

https://doi.org/10.1016/j.neuroimage.2020.116888
Received 4 February 2020; Received in revised form 26 April 2020; Accepted 26 April 2020
Available online 29 April 2020

access to myelin content, potentially improve specificity, and provide complementary information.

Therefore, dedicated short-T_2 techniques have been employed to image myelin based on the detection of its non-aqueous uT_2 signal (Wilhelm et al., 2012; Nayak et al., 2000; Waldman et al., 2003; Du et al., 2014; Seifert et al., 2017). Typically, sequences with radial centre-out k-space encoding and ultra-short echo time (UTE) or zero echo time (ZTE) are used (Weiger and Pruessmann, 2019). However, in all approaches presented so far, the timing of the MR sequence is not fully suited to comprehensively capture and sufficiently spatially encode the large portion of signals with T_2 below 100 μs. In particular, extended excitation pulses, echo times, gradient ramping, and/or readout times lead to considerable T_2-induced loss and/or blurring of such signals in the image (Seifert et al., 2017; Fan et al., 2018). An example of such a sequence is illustrated in Fig. 2b in relation to the decay of myelin lipid signal (Fig. 2a).

In the present work, advanced short-T_2 methodology and hardware (Froidevaux et al., 2020) is employed to image the majority of the uT_2 tissue components in the brain. The potential of the approach is demonstrated in excised porcine brain tissue and applied in vivo in a human volunteer.

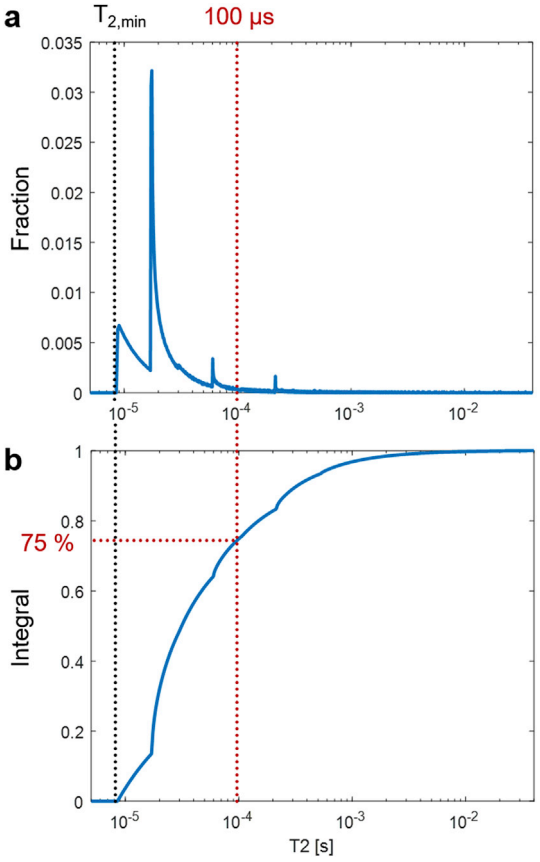

Fig. 1. Illustration of the distribution of T_2 values for the ^{1}H signal of myelin lipids, calculated according to Ref. (Wilhelm et al., 2012). Four components with super-Lorentzian lineshape, $T_{2,min}$ = 8.6, 30, 108, 265 μs, and fractions 0.743, 0.124, 0.111, 0.021 were used. a) Distribution of T_2 values. Each super-Lorentzian contributes with two prominent peaks appearing at $T_{2,min}$ and $2T_{2,min}$. The indicated onset of the very first peak corresponds to $T_{2,min}$ of the component with the fastest decay. b) Cumulative distribution obtained by integrating a), showing that 75% of the signal has T_2 values below 100 μs

2. Methods

2.1. Sequence

The two basic requirements for proper depiction of uT_2 components are (i) a short delay between radio-frequency (RF) excitation and acquisition (the RF dead time Δt), affecting the signal-to-noise ratio (SNR), and (ii) a short range within which k-space data are collected (the acquisition range T_k), affecting the actual spatial resolution (Weiger and Pruessmann, 2019). To meet these criteria, the three-dimensional (3D) ZTE-based hybrid filling (HYFI) technique (Froidevaux et al., 2019; Froidevaux and Weiger, 2019) was employed with minimised timing as shown in Fig. 2c. In the ZTE sequence, short-T_2 sensitivity is maximised by performing RF excitation only after ramping up the readout gradient. Therefore, data are missed during the RF dead time leading to a gap in central k-space. To fill this gap, HYFI efficiently collects additional data by using a combination of multiple radial readouts at lowered gradient strength and single-point imaging (SPI) (Emid and Creyghton, 1985; Balcom et al., 1996).

The time of acquisition for different k-space radii is illustrated for HYFI in Fig. 3: The very central data are obtained with SPI after the echo time[3] TE = Δt; during the radial HYFI parts, later acquisition is allowed within a certain duration t_{acq}; and the ZTE data collected at full gradient strength G determine T_k. Decreasing T_k reduces detrimental effects of T_2 decay on resolution and can be achieved by increasing G or Δt (Froidevaux et al., 2020). However, increasing Δt reduces the SNR efficiency as more signal decay is allowed to occur before data acquisition starts and because the scan time for the gap is increased. Increasing Δt to the reasonable maximum and setting $t_{acq} = 0$ leads to $T_k = dw$ (where dw is the Nyquist dwell time), a limiting case of HYFI which is equivalent to SPI with circular k-space support. Another limiting case is $t_{acq} = dw$, which fills the gap exclusively with SPI data and thus corresponds to the PETRA (pointwise encoding time reduction with radial acquisition) technique (Grodzki et al., 2012).

All protocols were designed with 3D isotropic geometry, and their sequence parameters are listed in Table 1. For each task, they were chosen such as to approach a desired actual resolution at useful SNR and scan time within limits of maximally available G and minimum possible Δt. The RF pulse power was adjusted to provide maximum steady-state signal in WM. However, in vivo the optimal flip angle could not be used due to limits of specific absorption rate (SAR), resulting in an unusually small excitation of approximately 1°, which is still reasonable at a repetition time (TR) as short as 1 ms. To observe signal decay or create contrast, T_2^* weighting was introduced in the HYFI sequence by increasing Δt (and thus TE) and reducing the gradient strength according to the chosen k-space gap.

2.2. Hardware

The demanding timing requirements for uT_2 imaging were met by employing advanced, dedicated hardware. A 3T Achieva MRI system (Philips Healthcare, The Netherlands) was equipped with a high-performance gradient insert suitable for head and extremity imaging, which provides a maximum strength of 200 mT/m with a slew rate of 600 mT/m/ms at 100% duty cycle (Weiger et al., 2018). RF operation was performed using a custom-built RF chain (Weiger et al., 2013), including rapid transmit-receive switches (Brunner et al., 2016), a high-bandwidth spectrometer (Dietrich et al., 2016), and proton-free loop and birdcage coils (Rösler et al., 2016, 2017).

[3] Note that although no actual echo is created in the employed sequences, TE is provided as the time when k = 0 is acquired. This corresponds to the definition for echo-based techniques and the common use in literature on UTE imaging.

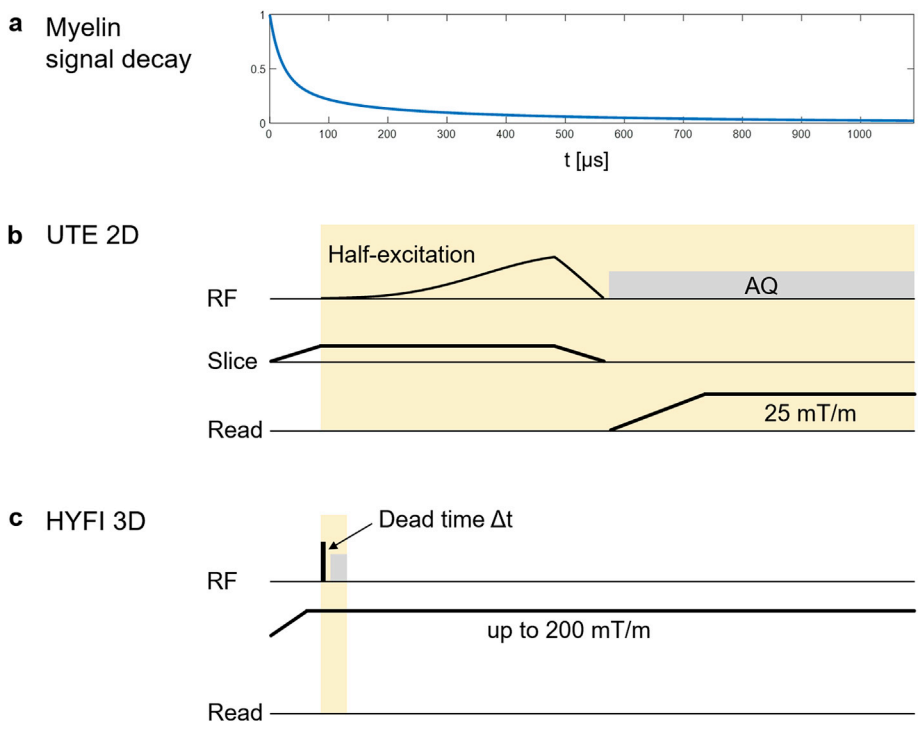

Fig. 2. Radial short-T_2 MRI sequences used for depiction of the uT_2 tissue components in myelin. a) Super-exponential decay of myelin lipid signal. It corresponds to the T_2 distribution in Fig. 1a, from which T_2 values and fractions were taken to create a sum of exponential decays. This plot serves as a time basis but directly aligning the signal with the sequences is not possible since the effect of extended RF excitation depends on T_2. b) Typical two-dimensional (2D) ultra-short echo time (UTE) sequence as used, e.g., in Ref. (Sheth et al., 2016), with half-pulse radio-frequency (RF) excitation of duration 472 µs, a gradient ramp of duration 167 µs, and a readout gradient strength of 25 mT/m c) Three-dimensional (3D) zero echo time–based technique with hybrid filling (HYFI) as employed in the present work. RF excitation is performed only after the readout gradient of amplitude up to 200 mT/m has been switched on. In this way, only a short initial range of the decay is covered. With HYFI, additional data for the central k-space locations missed during the RF dead time between excitation and acquisition are efficiently collected with a combination of multiple radial acquisitions at lowered gradient strength and single-point imaging.

2.3. Samples and subjects

The ability to image uT_2 tissue components was investigated in two samples excised from porcine brain in which the size of GM and WM structures is comparable to humans (Welker et al., 1990). The fresh brain of an adult pig was obtained from the local slaughterhouse and frozen. Before scanning, pieces of 3 mm thickness and 30 mm diameter were cut and thawed. In one of the samples, to largely remove long-T_2 signals, water was exchanged with deuterated water. This sample was continuously immersed in a fresh 10-ml solution of 99.8% D_2O for 20 h, three successive times, for a total of 60 h (Wilhelm et al., 2012).

In-vivo feasibility of the imaging approach was tested in the brain of one healthy human subject according to applicable ethics approval and with written informed consent.

2.4. Data processing

From a series of SPI scans with 13 TE values performed on each of the two tissue samples (protocol 4, Table 1), the signal decay was evaluated by means of a fitting procedure. Initially, due to the low matrix size, tricubic interpolation was applied to each of the 3D images, thus reducing the voxel size by a factor of two. Locations with intensities below 10% of the maximum in the shortest-TE image were excluded. The signal evolution was approximated by a complex-valued model (Nam et al., 2015; Boucneau et al., 2018) of three components with Lorentzian (L) or super-Lorentzian (SL) lineshapes

$$S(TE) = e^{i(\phi+\Delta\omega TE)} \sum_{c=1}^{3} a_c D_c\left(T^*_{2,c}\middle|T^*_{2,min,c}\right) e^{i\delta_c\omega_0 TE}, \quad [1]$$

where ϕ is an arbitrary global phase, $\Delta\omega$ is (local) off-resonance, ω_0 is the ^{1}H Larmor frequency, and each component is characterised by its amplitude fraction a, chemical shift δ, and decay function D. The latter is either exponential or super-exponential and determined by T_2* or T_2*$_{,min}$ respectively, where the * notation indicates that experimental values in principle also reflect decay from local B0 inhomogeneity. For fitting this model, a nonlinear least-squares algorithm was used.

In a first step, data from the D_2O-exchanged sample were averaged over 33 WM pixels (selected from regions of highest signal intensity) and fitted with two SL and one L component with $\delta = 4.70$ ppm and $T_2^* = 50$ ms. The last component represents mobile water, which cannot be characterised well with the relatively small TE values used. In a second step, pixel-wise fitting was performed on both tissue samples where, to stabilise the procedure, all results from the first fit were adopted apart from amplitudes a and local off-resonance $\Delta\omega$. In this way, 3D component maps were obtained.

In-vivo data obtained with shortest and increased TE (protocols 5 and 6, Table 1) were compared by magnitude subtraction, thus creating an image where short-T_2* signals are emphasised. Before subtraction, the two data sets were 3D rigid body–registered to reduce motion effects. Negative values in the subtraction data were assigned to artefacts related to motion, flow, or spoiling inconsistency (Hargreaves, 2012) and therefore set to zero.

Plausibility of the signal decay observed in vivo was tested with a simple two-component model consisting of total water signal S_w, unaffected by prolonging TE, and the uT_2 signal S_u, experiencing decay described by a factor D. Thus, magnitude signals at short and long TE are $S_S = S_w + S_u$ and $S_L = S_w + D\,S_u$. As no detailed information is currently available for all the uT_2 components involved, the overall decay factor D was estimated from the model in Eq. [1] using the parameters found by fitting the tissue data. At known D, the two-component enabled calculation of the total water signal fraction $S_w/(S_w + S_u)$.

2.5. Simulations

Simulations were performed to investigate the depiction quality of the sequences in Fig. 2 for uT_2 components. The effect of T_2 decay during the RF pulse was determined by Bloch simulations for on-resonant spins, and is given by the relative transverse magnetisation with respect to that obtained for infinite T_2. k-Space data for spheres of different size were calculated analytically (Koay et al., 2007), which is both accurate and fast, and weighted with the T_2 decay of myelin lipids (see Fig. 2a) according to the respective acquisition scheme (see Fig. 3). Possible differences in detectable magnetisation (related to e.g. repetition time, nominal flip angle, or preparation pulses) or in noise levels (related to e.g. bandwidth or image subtraction) were not considered here and assumed equal for all

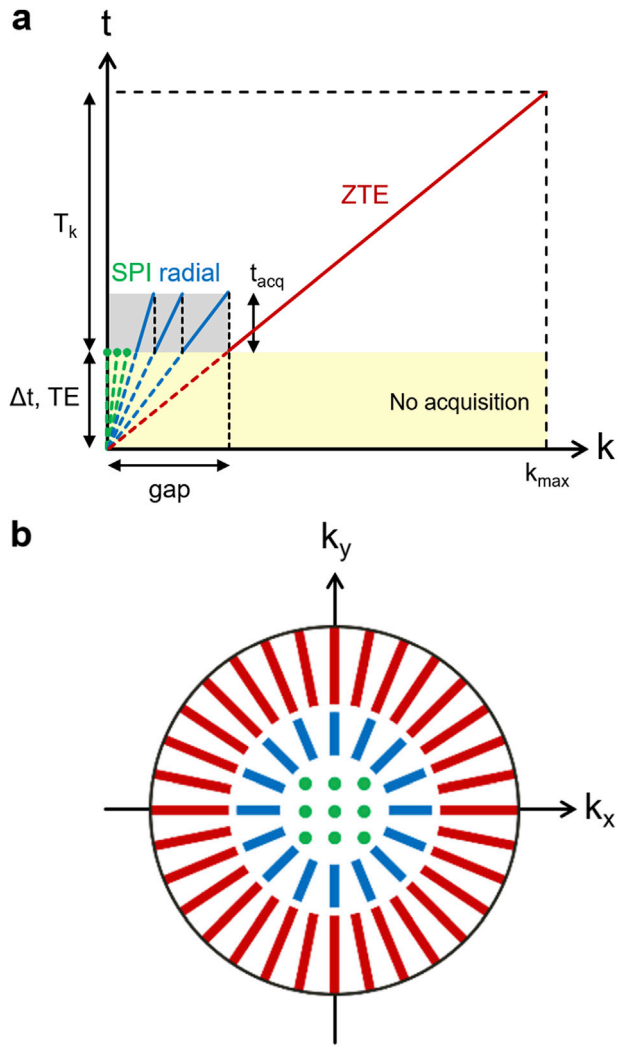

Fig. 3. k-Space scheme of the HYFI sequence in Fig. 2c. a) Relation of time and k-space. The time of acquisition t of the data is plotted as a function of the k-space radius k. The technique is based on ZTE imaging, where radial centre-out encoding is performed and data are acquired at the earliest after the RF dead time Δt. Data missed during Δt (yellow-shaded range, dashed lines) lead to a gap in central k-space, which in the HYFI approach is filled with multiple sets of radial readouts of decreasing gradient amplitudes followed by SPI in the very centre. The acquisition duration t_{acq} of HYFI (grey-shaded region) is selected as a compromise between scan efficiency and the maximum decay accepted for a targeted T_2. The total range of acquisition T_k is an indicator for the resolution loss expected for a given T_2. T_k can be reduced by increasing the gradient strength or Δt. As data at lower k values dominate the contrast, the echo time TE of the sequence is considered equal to Δt: More accurately, $TE = \Delta t + dw/2$, where $dw = 1/bw$ is the Nyquist dwell time corresponding to the bandwidth bw within the field of view. Note that the plot also includes as limiting cases PETRA (for $t_{acq} = dw$) and SPI (for $T_k = t_{acq} = dw$). b) Illustration of acquisition pattern in 3D k-space, from which a central 2D slice is shown. Colours indicate the different parts of the acquisition described in a). Abbreviations: HYFI = hybrid filling, ZTE = zero echo time, SPI = single-point imaging, PETRA = pointwise encoding time reduction with radial acquisition.

simulations.

3. Results

3.1. Simulations

The simulation results are shown in Fig. 4. The UTE sequence with extended timing from Fig. 2b exhibits considerable T_2-induced relative signal loss, with a reduction to 87% after the RF pulse and 27% in the final image. In addition, significant blurring is observed, which leads to an image background (Fig. 4b and d). Furthermore, retracing mono-exponential fitting to data obtained with TE = 8, 200, and 600 μs from Ref. (Sheth et al., 2016) leads to an apparent T_2 of 300 μs (Fig. 4e), which is comparable to the results reported in the publication. Using instead the optimised HYFI technique of Fig. 2c, higher relative signal (64%) and much sharper depiction is obtained (Fig. 4c).

Table 1
Sequence parameters of the six protocols used for isotropic three-dimensional imaging of the uT_2 components in the brain. SPI: single point imaging; HYFI: zero echo time imaging with hybrid filling; FOV: field of view; G: gradient strength; bw: bandwidth in the FOV; dw: Nyquist dwell time = $1/bw$; Δt: dead time; TE: echo time; T_k: acquisition range; t_{acq}: HYFI acquisition duration; TR: repetition time. See Fig. 3 for details about timing parameters.

Subject	Excised porcine brain tissue				Human in vivo	
Protocol	1	2	3	4	5	6
Method	HYFI	HYFI	HYFI	SPI	HYFI	HYFI
FOV [mm]	50	50	50	50	260	260
Matrix	128	128	128	32	150	150
Nominal resolution [mm]	0.39	0.39	0.39	1.56	1.73	1.73
G [mT/m]	40	200	200	200–3.5	181	14
bw [kHz]	85	425	425	425–7.5	2000	157
dw [μs]	11.8	2.4	2.4	2.4–133	0.5	6.4
Δt [μs]	10	10	50	35–2066	15	457
TE [μs]	15.9	11.2	51.2	36–2133	15	460
T_k [μs]	743	141	101	2.4–133	29	27
t_{acq} [μs]	22	22	22	0	0	27
Pulse type + duration [μs]	Hard 2	Hard 2	Hard 2	Hard 2	Sweep 12	Sweep 12
TR [ms]	1	1	1	3	1	1
Averages	7	16	32	1	10	1
Scan time [m:s]	6:00	13:55	40:22	0:53	32:40	12:50
Slices averaged for display	2	2	2	1	3	3

3.2. Tissue samples

Fig. 5 demonstrates high-resolution imaging of uT_2 tissue components using the D_2O-exchanged sample. In the image obtained with a conventional gradient strength of 40 mT/m, grey matter (GM) and WM can be distinguished, but blurring is observed (Fig. 5a). The blurring is considerably reduced at 200 mT/m (Fig. 5b), and the image is further sharpened by increasing the dead time (Fig. 5c). Note that for these two steps, averaging was increased to compensate for higher bandwidth and stronger signal decay respectively. From the observed improvement in actual resolution it can be concluded that the majority of the signal present in the sample originates from uT_2 tissue components.

To further investigate the signal characteristics of the sample, a series of SPI acquisitions with increasing TE was performed. SPI is advantageous for quantitative analysis as all k-values for one image are obtained at identical Δt, but it requires a trade-off between shortest TE and resolution. In the obtained data, rapid signal decay is observed as TE increases (Fig. 6a). Fitting the model of Eq. [1] to the averaged WM values in Fig. 7a results in the three signal components listed in Table 2. The signal is dominated by a SL component with $T_2^{*}{}_{,min} = 7.5$ μs which has previously been assigned to methylene protons in myelin lipids (Wilhelm et al., 2012). A second, weaker SL component has a longer $T_2^{*}{}_{,min} = 101$ μs, and the L component represents residual water with incomplete exchange. Importantly, the different chemical shifts are reflected in the signal phase, where the lipid frequency dominates for short TE and the water frequency takes over at longer TE (Fig. 7b). In the amplitude maps obtained by pixel-wise fitting (Fig. 6b), the short SL is most characteristic for WM, indicating a large contribution from myelin lipids whereas the other two components exhibit considerably less contrast.

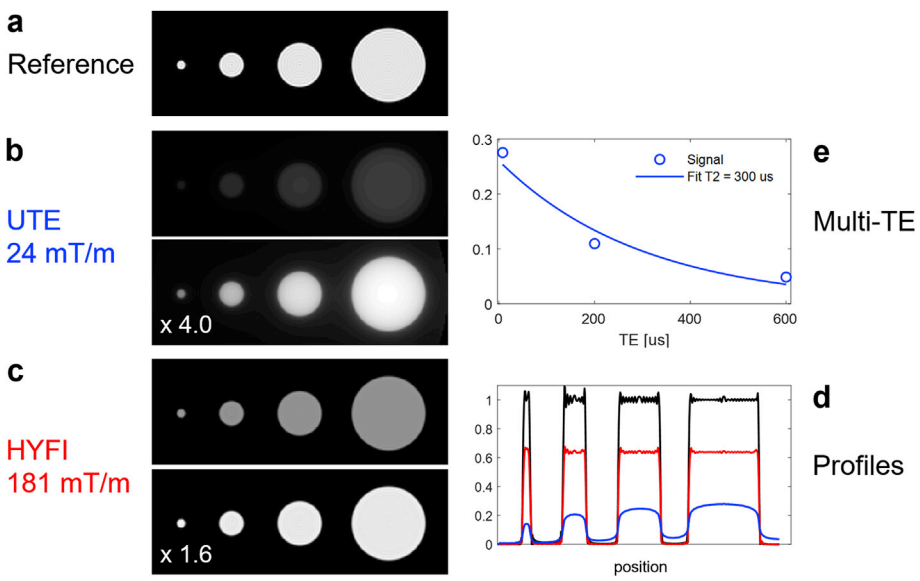

Fig. 4. Simulation of the effects of T_2 decay on relative signal yield and spatial resolution for imaging of the myelin lipid components according to Fig. 2. The simulation considers the effect of signal decay during excitation as well as before and during acquisition. Not included are possible differences in detectable magnetisation (e.g. related to repetition time, flip angle, or preparation pulses) or noise levels (e.g. related to bandwidth or image subtraction). Final signal values were determined in the central part of the largest sphere. a) The reference image without any effects from signal decay exhibits common Gibbs ringing. b) For ultra-short echo time (UTE) imaging with conventional gradient strength of 25 mT/m, the relative signal amplitude is considerably reduced. Moreover, signal blurring is observed in the image with up-scaled intensity. c) Using for the same geometry the hybrid filling (HYFI) technique with protocol 5 in Table 1 and a maximum gradient strength of 196 mT/m, less signal reduction and blurring occur. d) Horizontal profiles through the images confirm these observations. e) Mono-exponential fitting of multi-TE UTE data as in Ref. (Sheth et al., 2016) leads to a comparable T_2 value of 300 μs.

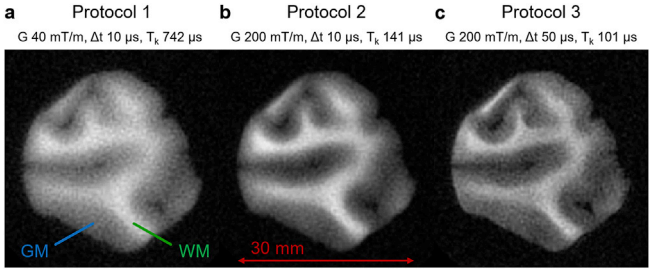

Fig. 5. Short-T_2 imaging of excised porcine brain tissue using the hybrid-filling (HYFI) technique with protocols listed in Table 1. Through D_2O-exchange, long-lived water was largely removed from the sample, leaving primarily the uT_2 components. a) The image acquired at conventional gradient strength G shows contrast between white matter (WM) and grey matter (GM), but is blurred. b) Shortening the acquisition range by a five-fold increase of G leads to sharper depiction and stronger contrast, indicating that mainly uT_2 components are present. c) This effect is further enhanced by deliberately increasing the dead time Δt, thus reducing T_k (see Fig. 3).

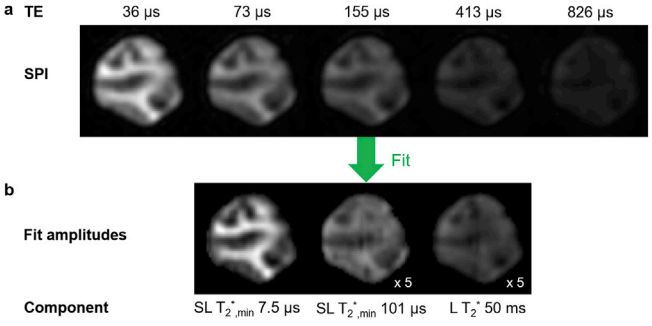

Fig. 6. Single-point imaging (SPI) of D_2O-exchanged porcine brain tissue with multiple echo times (TE) using protocol 4 of Table 1. a) With increasing TE, rapid signal decay is observed, confirming a dominating contribution from uT_2 tissue components. b) Fitting the signal evolution (see Fig. 7) provides amplitude maps for three components. The most rapidly decaying component exhibits strong contrast between grey and white matter. SL: Super-Lorentzian, L: Lorentzian.

Fig. 8 shows the equivalent results for the non-exchanged sample. Here, long-lived water signal dominates the images, leading to conventional T_1 contrast and comparable sharpness for all three high-resolution protocols (Fig. 8a). Nevertheless, a signal reduction is observed in WM at larger TE (Fig. 8b), indicating detection of uT_2 signals at shortest TE. This is confirmed by the subtraction of the two images, which provides good WM-GM contrast. Similar but stronger contrast is observed in the fitted amplitude map of the short SL component (Fig. 8c), comparable to the D_2O-exchanged sample. The maps of the longer SL and the water component clearly exhibit lower contrast, where the SL map partly suffers from B0 inhomogeneity and low signal amplitude.

3.3. *In vivo*

To demonstrate in-vivo feasibility of the presented approach for imaging uT_2 tissue components in the brain, a protocol was chosen with small Δt and T_k, a resolution just suitable to distinguish GM and WM structures, and a manageable scan time. For the additional long-TE image the HYFI gap fully covered the k-space support to obtain a flat T_2^* weighting, resulting in benign depiction properties after image subtraction while still keeping scan time contained. The short-TE image shows negligible contrast between WM and GM (Fig. 9a). Due to SAR limits the applied flip angle did not provide maximum steady-state magnetisation, such that mainly proton density contrast with little T_1 weighting is expected. Hence, equal intensity for WM and GM indicates that the lower water content in WM is compensated by capturing the uT_2 components. This is confirmed by clearly reduced WM signal in the long-TE image (Fig. 9b). In contrast, increased signal is obtained for cerebrospinal fluid, which is likely due to a reduced spoiling efficiency at lower gradient strength (Hargreaves, 2012). In the short-T_2^*-enhanced subtraction image (Fig. 9c), prominent signal is observed from the skull, the skin, and the ear muffs. In the brain, clear contrast is present between WM and GM, which according to the observations in the raw images and in the tissue data is associated with the uT_2 components in WM.

Signal values over a deep WM region of interest in the second-row images of Fig. 9 show a reduction of 23% at longer TE. By using the two-component model from section 2.4, a total water signal fraction of 73% was estimated, which reflects common values of water content reported for brain WM (Adachi and Feigin, 1966; O'Brien and Sampson, 1965).

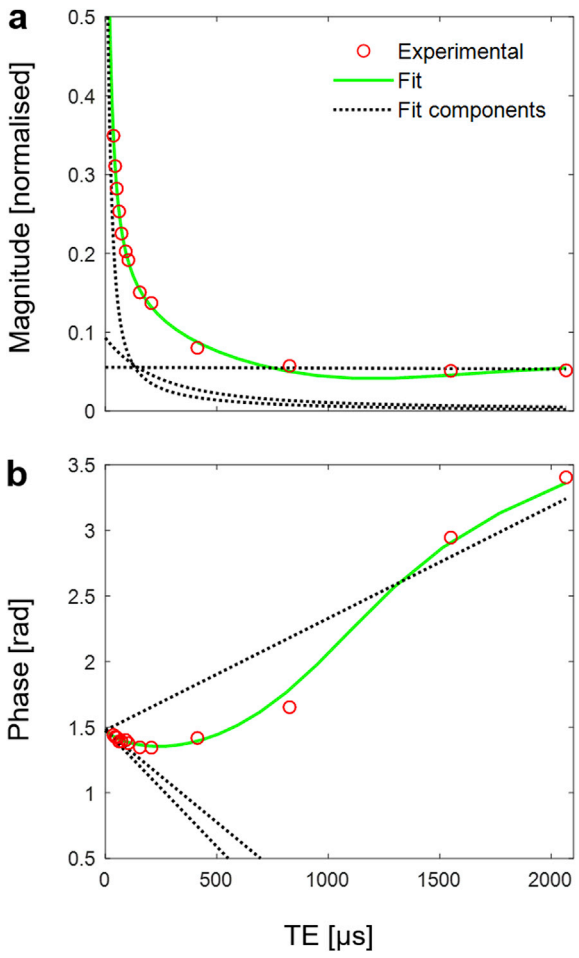

Fig. 7. Signal evolution and fit of the image series in Fig. 6a. Experimental data was averaged over 33 white matter pixels. a) Magnitude and b) phase show non-exponential and non-linear behaviour, respectively. The data were fitted using the complex-valued model in Eq. [1] with three signal components (dotted lines), resulting in the values listed in Table 2. Two rapidly decaying components with lipid-typical chemical shifts dominate at short echo times (TE), whereas the long-lived water component governs the behaviour at larger TE. This composition leads to the curved phase behaviour and the slightly increased magnitude at later times. Using the found components, the amplitude maps in Fig. 6b were obtained by pixel-wise fitting of the images in Fig. 6a.

4. Discussion

In this study, the feasibility of depicting the myelin bilayer with MRI was explored. It was found that the non-aqueous tissue components in the CNS can indeed be well-resolved despite extremely rapid signal decay. This was enabled by advanced short-T_2 methodology and hardware, in particular a high-performance gradient. The approach was successfully applied in both excised tissue and the human brain.

As the final aim is quantitative depiction of myelin content, it is important to understand to which degree the observed signal reflects the target tissue. Contributions to the uT_2 signal stem from lipids and proteins not only in myelin, but also in axon and glial cell membranes (Wilhelm et al., 2012). Apart from myelin lipids, the embedded proteins can also be considered characteristic of the myelin bilayer. Furthermore, a significant portion of the glia is oligodendrocytes, which form the myelin sheath (Morell et al., 1999) and could therefore be seen as part of it. In this sense, a large fraction of the uT_2 signal is associated with myelin content, and remaining non-myelin signal may be treated as a baseline. However, the validity of this interpretation depends on the role of the different contributions in disease-related demyelination (Popescu and Lucchinetti, 2012) and will need further consideration.

Alternatively, instead of evaluating the uT_2 signal as a whole, individual components may be separated. In the present work, this was accomplished on multi-TE data obtained from excised tissue by fitting a three-component model. Based on previous findings (Wilhelm et al., 2012), the shortest-lived signal could convincingly be assigned to the methylene groups in myelin lipids. The longest-lived component summarises any signals that decay negligibly during the relatively short delay of about 2 ms, hence mainly myelin water as well as more mobile intra- and extracellular water. The decay properties of the intermediate component approximately match other contributions from myelin lipids (Wilhelm et al., 2012), but may also reflect proteins and similar signals from glial cells (Bloom et al., 1969). Only three components were used because fitting multi-exponential functions is notoriously badly conditioned. In this respect, stabilisation was obtained due to the presence of different chemical-shift off-resonances, leading to more numerically

Table 2
Results from fitting the experimental data in Fig. 7 using the model in Eq. [1]. Three signal components were used, and the parameters marked with an † were held at constant values during the fit. Standard errors on fitted parameters are given in brackets, obtained by propagation of the noise variance in the underlying images. The mean-normalised root-mean-square error of the fit was 0.037.

Component	Type	T_2^* or $T_{2,min}^*$	Chem. shift	Amplitude fraction
1	SL	7.5 (0.8) μs	1.38 (0.11) ppm	0.85 (0.08)
2	SL	101 (5) μs	1.91 (0.06) ppm	0.09 (0.00)
3	L	50 ms†	4.70 ppm†	0.06 (0.00)

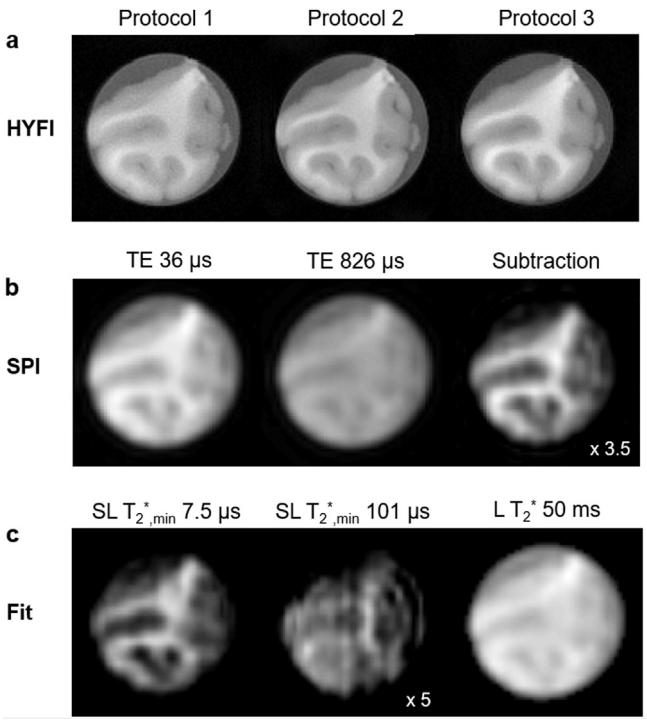

Fig. 8. Short-T_2 imaging of excised porcine brain tissue without D_2O exchange by analogy with Figs. 5 and 6. a) High-resolution imaging with the hybrid filling (HYFI) technique: Shortening the acquisition range with protocol 2 and increasing the k-space plateau with protocol 3 does not notably change image resolution compared to protocol 1 as long-T_2 water dominates both images. b) Nevertheless, single-point imaging (SPI) data at long echo time (TE) shows reduced white matter signal, indicating decay of the uT_2 tissue components. Direct subtraction (short- minus long-TE image) provides contrast between white and grey matter in agreement with a). c) The fitted amplitude of the very short-lived super-Lorentzian (SL) component clearly reflects locations of white and grey matter, whereas both the longer SL and the water component exhibit low contrast.

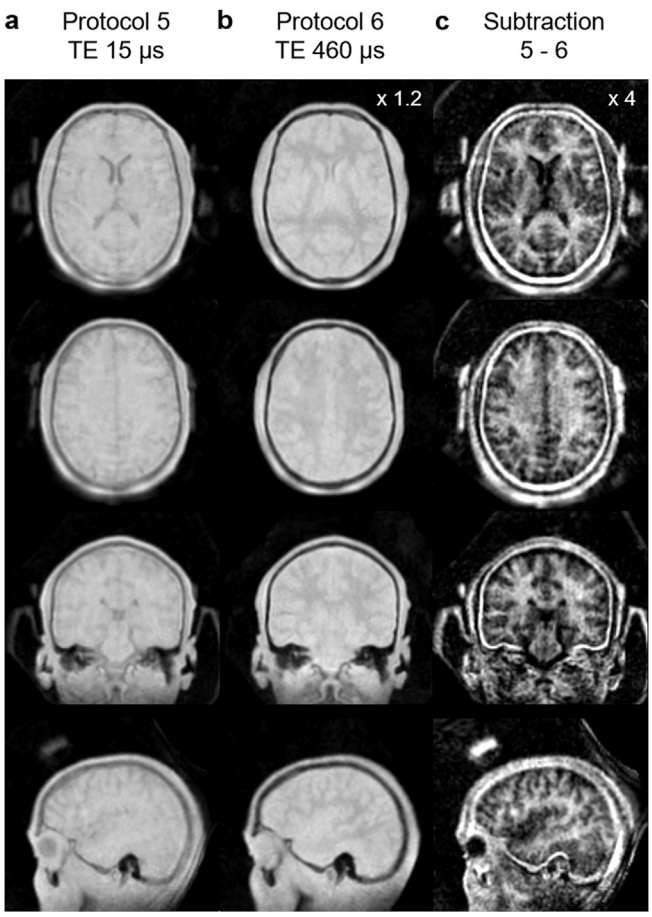

Fig. 9. In-vivo imaging of the uT_2 tissue components in the human brain using the hybrid filling (HYFI) technique with the protocols listed in Table 2. Selected, orthogonal views from a three-dimensional isotropic data set are shown. a) The image acquired with an echo time (TE) of 15 µs and a short acquisition range of 29 µs shows little grey-white matter contrast. b) Increasing TE leads to visibly reduced signal in white matter. c) Subtraction of the two data sets largely removes long-lived signal, showing predominantly the uT_2 components with clear contrast between grey and white matter. Other short-lived signals visible in the images can be assigned to the skull, skin, and ear muffs.

benign linear phase evolutions in the signal. To fully exploit the potential of the fitting approach, further investigation is needed concerning optimal sequence parameters as well as number and properties of components.

The uT_2 components were also depicted in the human brain. As only one longer-TE image was acquired no model fitting was performed, but subtraction images were created, which were shown to provide similar information as in the analysis of the tissue data. Current restrictions to probing more than two TEs arise from long scan times due to relatively low SNR. One reason for the latter is the large power deposited by the high-bandwidth RF pulses, which due to SAR limits lead to a sub-optimal flip angle. Nevertheless, SNR increase is expected from an improved RF setup (separate transmit and receive coils), sequence optimisation (SNR-maximised scheme for bandwidth, TE, averaging, and HYFI parameters), and higher field strength, thus potentially enabling also a multi-TE approach at reasonable scan times.

Short-T_2 signals have also been targeted in previous work with sequence timings potentially less suitable for the rapid decay occurring in myelin lipids (Du et al., 2014; Boucneau et al., 2018). In such studies, mono-exponential decay constants of hundreds of microseconds were found, thus raising debate about the discrepancy of the results (Fan et al., 2018). Some light is shed on this question by the simulations shown in Fig. 4, where an approach with extended timing does indeed detect the myelin signal with an apparent T_2 comparable to the reported values. However, the relative amplitude is considerably reduced and a degree of blurring is observed that may seriously hamper quantification. Another source of potential contamination in previous approaches is out-of-slice signal from distorted shapes of half-excitation pulses due to rapid transverse relaxation (Robson and Gatehouse, 2010) and eddy currents (Wansapura et al., 2001; Josan et al., 2009). A further controversial topic is the use of inversion-recovery preparation for suppressing long-T_2 signals based on T_1 and T_2 differences with respect to uT_2 myelin components (Du et al., 2014). Such sequences suffer from limited acquisition duty cycle and also considerably reduce uT_2 signals. Moreover, suppression efficiency strongly depends on T_1 and inversion times and has been found to provide limited reliability (Harkins and Does, 2019).

On the other hand, UTE-based approaches are usually not limited with respect to flip angles and can operate at optimum steady-state magnetisation. Furthermore, using lower gradients means lower bandwidth and hence lower noise levels. These two aspects, which were not considered in the present work, may explain the relatively high SNR of image regions assigned to myelin in the previous studies. Another advantage of UTE lies in offering both 2D and 3D geometry, and the sequence can certainly also benefit from using high-performance gradients. Hence, finding the best compromise between SNR efficiency and spatial resolution will require a comprehensive investigation which takes into account all sequence options and parameters. This may be accomplished by including neglected aspects into the simulation used in the present work.

A general challenge in the development and verification of techniques for the detection of myelin is the availability of a suitable phantom allowing quantitative and reproducible measurements. The exact composition of any individual tissue sample can only partially be known from literature (Morell et al., 1999). Furthermore, decomposition occurs at room temperature, and both freezing and fixation change tissue properties (Seifert et al., 2019). To simplify MR signal composition, H_2O of long T_2 can be largely replaced by D_2O through a relatively straightforward procedure. Considerably more effort and expertise is required to create purified myelin lipid extract (Wilhelm et al., 2012). Related products can also be purchased from commercial sources (e.g. Sigma-Aldrich Corp, St. Louis, MO) (Sheth et al., 2016), but are very expensive and may show structural properties diverging from living tissue (Reichert et al., 2019). As a promising independent way of relating MR image intensities to myelin content in excised tissue, it has been suggested to use luxol fast blue staining (Laule et al., 2008), but staining results are very sensitive to variations in the procedure.

The role of imaging the uT_2 components within the group of existing MR-based methods targeting myelin is yet to be found. Insights are expected from direct comparisons. Relating actual detection of non-aqueous protons to indirect approaches using magnetisation transfer would be of particular interest. Direct access to the macromolecular pools may also contribute to improving the associated exchange models.

5. Conclusion

It has been demonstrated that signals in the CNS with ultra-short T_2 can be depicted with MRI by means of advanced hardware and methodology. As a large fraction of these signals reflects myelin content, the approach has strong potential to improve research and diagnosis of diseases involving demyelination. Future research should focus on further technical improvements, protocol optimisation, as well as verification and broader application of the method.

CRediT authorship contribution statement

Markus Weiger: Conceptualization, Methodology, Software, Formal analysis, Investigation, Writing - original draft, Visualization. **Romain Froidevaux:** Conceptualization, Methodology, Software, Resources, Investigation, Writing - review & editing, Visualization. **Emily Louise**

Baadsvik: Software, Formal analysis, Validation, Writing - review & editing. **David Otto Brunner:** Resources. **Manuela Barbara Rösler:** Resources, Writing - review & editing. **Klaas Paul Pruessmann:** Conceptualization, Writing - review & editing, Supervision, Funding acquisition.

References

Adachi, M., Feigin, I., 1966. Cerebral oedema and the water content of normal white matter. J. Neurol. Neurosurg. Psychiatr. 29, 446–450.

Balcom, B.J., MacGregor, R.P., Beyea, S.D., Green, D.P., Armstrong, R.L., Bremner, T.W., 1996. Single-point ramped imaging with T1 enhancement (SPRITE). J. Magn. Reson., Ser. A 123, 131–134.

Bloom, M., Holmes, K.T., Mountford, C.E., Williams, P.G., 1969. Complete proton magnetic resonance in whole cells. J. Magn. Reson. 69, 73–91, 1986.

Bloom, M., Burnell, E.E., Roeder, S.B.W., Valic, M.I., 1977. Nuclear magnetic resonance line shapes in lyotropic liquid crystals and related systems. J. Chem. Phys. 66, 3012–3020.

Boucneau, T., Cao, P., Tang, S., Han, M., Xu, D., Henry, R.G., Larson, P.E.Z., 2018. In vivo characterization of brain ultrashort-T2 components. Magn. Reson. Med. 80, 726–735.

Brunner, D.O., Furrer, L., Weiger, M., Baumberger, W., Schmid, T., Reber, J., Dietrich, B.E., Wilm, B.J., Froidevaux, R., Pruessmann, K.P., 2016. Symmetrically biased T/R switches for NMR and MRI with microsecond dead time. J. Magn. Reson. 263, 147–155.

Dietrich, B.E., Brunner, D.O., Wilm, B.J., Barmet, C., Gross, S., Kasper, L., Haeberlin, M., Schmid, T., Vannesjo, S.J., Pruessmann, K.P., 2016. A field camera for MR sequence monitoring and system analysis. Magn. Reson. Med. 75, 1831–1840.

Du, J., Ma, G., Li, S., Carl, M., Szeverenyi, N.M., VandenBerg, S., Corey-Bloom, J., Bydder, G.M., 2014. Ultrashort echo time (UTE) magnetic resonance imaging of the short T2 components in white matter of the brain using a clinical 3T scanner. Neuroimage 87, 32–41.

Emid, S., Creyghton, J., 1985. High resolution NMR imaging in solids. Phys. B+C 128, 81–83.

Fan, S.J., Ma, Y., Zhu, Y., Searleman, A., Szeverenyi, N.M., Bydder, G.M., Du, J., 2018. Yet more evidence that myelin protons can be directly imaged with UTE sequences on a clinical 3T scanner: bicomponent T2* analysis of native and deuterated ovine brain specimens. Magn. Reson. Med. 80, 538–547.

Froidevaux, R., Weiger, M., 2019. Magnetic Resonance Imaging Method with Hybrid Filling of K-Space. Patent W0/2019/072778.

Froidevaux, R.N., Rösler, M.B., Brunner, D.O., Weiger, M., Pruessmann, K.P., 2019. HYFI: hybrid filling of the dead-time gap for faster zero echo time imaging. In: Proceedings of the 27th Annual Meeting of ISMRM. Canada, Montreal, p. 943.

Froidevaux, R., Weiger, M., Rosler, M.B., Brunner, D.O., Dietrich, B.E., Reber, J., Pruessmann, K.P., 2020. High-resolution short-T2 MRI using a high-performance gradient. Magn. Reson. Med. https://doi.org/10.1002/mrm.28254.

Gass, A., Barker, G.J., Kidd, D., Thorpe, J.W., MacManus, D., Brennan, A., Tofts, P.S., Thompson, A.J., McDonald, W.I., Miller, D.H., 1994. Correlation of magnetization transfer ration with clinical disability in multiple sclerosis. Ann. Neurol. 36, 62–67.

Glasser, M.F., Van Essen, D.C., 2011. Mapping human cortical areas in vivo based on myelin content as revealed by T1- and T2-weighted MRI. J. Neurosci. 31, 11597–11616.

Grodzki, D.M., Jakob, P.M., Heismann, B., 2012. Ultrashort echo time imaging using pointwise encoding time reduction with radial acquisition (PETRA). Magn. Reson. Med. 67, 510–518.

Hargreaves, B., 2012. Rapid gradient-echo imaging. J. Magn. Reson. Imag. 36, 1300–1313.

Harkins, K.D., Does, M.D., 2019. Myelin UTE imaging, to be or not to be?. In: Proceedings of the 27th Annual Meeting of ISMRM, Montreal, Canada, p. 4895.

Horch, R.A., Gore, J.C., Does, M.D., 2011. Origins of the ultrashort-T2 1H NMR signals in myelinated nerve: a direct measure of myelin content? Magn. Reson. Med. 66, 24–31.

Josan, S., Kaye, E., Pauly, J.M., Daniel, B.L., Pauly, K.B., 2009. Improved half RF slice selectivity in the presence of eddy currents with out-of-slice saturation. Magn. Reson. Med. 61, 1090–1095.

Koay, C.G., Sarlls, J.E., Ozarslan, E., 2007. Three-dimensional analytical magnetic resonance imaging phantom in the Fourier domain. Magn. Reson. Med. 58, 430–436.

Laule, C., Vavasour, I.M., Kolind, S.H., Li, D.K.B., Traboulsee, T.L., Moore, G.R.W., MacKay, A.L., 2007. Magnetic resonance imaging of myelin. Neurotherapeutics 4, 460–484.

Laule, C., Kozlowski, P., Leung, E., Li, D.K., Mackay, A.L., Moore, G.R., 2008. Myelin water imaging of multiple sclerosis at 7 T: correlations with histopathology. Neuroimage 40, 1575–1580.

Lawson, K.D., Flautt, T.J., 1965. Nuclear magnetic resonance absorption in anhydrous sodium soaps. J. Phys. Chem. 69, 4256–4268.

Love, S., 2006. Demyelinating diseases. J. Clin. Pathol. 59, 1151–1159.

MacKay, A., Whittall, K., Adler, J., Li, D., Paty, D., Graeb, D., 1994. In vivo visualization of myelin water in brain by magnetic resonance. Magn. Reson. Med. 31, 673–677.

Morell, P., Quarles, R.H., 1999. Myelin formation, structure and biochemistry. In: Siegel, G., Agranoff, B., Albers, R., al, e (Eds.), Basic Neurochemistry: Molecular, Cellular and Medical Aspects, sixth ed. Lippincott-Raven, Philadelphia.

Nam, Y., Lee, J., Hwang, D., Kim, D.-H., 2015. Improved estimation of myelin water fraction using complex model fitting. Neuroimage 116, 214–221.

Nayak, K.S., Pauly, J.M., Gold, G.E., Nishimura, D.G., 2000. Imaging ultra-short T2 species in the brain. In: Proceedings of the 8th Annual Meeting of ISMRM, Denver, USA, p. 509.

O'Brien, J.S., Sampson, E.L., 1965. Lipid composition of the normal human brain: gray matter, white matter, and myelin. J. Lipid Res. 6, 537–544.

Popescu, B.F.G., Lucchinetti, C.F., 2012. Pathology of demyelinating diseases. Annu. Rev. Pathol. 7, 185–217.

Ramani, A., Aliev, A., Barker, G., Tofts, P., 2003. Another approach to protons with constricted mobility in white matter: pilot studies using wideline and high-resolution NMR spectroscopy. Magn. Reson. Imag. 21, 1039–1043.

Reichert, W.T., Pham, Q.D., Does, M.D., Topgaard, D., 2019. Evaluation of bovine brain extract phantom structure through polarization transfer solid-state NMR. In: Proceedings of the 27th Annual Meeting of ISMRM, Montreal, Canada, p. 2278.

Robson, M.D., Gatehouse, P.D., 2010. Consequences of T2 relaxation during half-pulse slice selection for ultrashort TE imaging. Magn. Reson. Med. 64, 610–615.

Rösler, M.B., Weiger, M., Schmid, T., Brunner, D.O., Froidevaux, R., Pruessmann, K.P., 2016. Ultrasonic soldering on glass for the construction of MRI coils with minimized background signal in short-T2 images. In: Proceedings of the 33rd Annual Scientific Meeting of ESMRMB, Vienna, Austria, p. 87.

Rösler, M.B., Weiger, M., Brunner, D.O., Schmid, T., Froidevaux, R., Pruessmann, K.P., 2017. An RF birdcage coil designed for an insert gradient coil dedicated to short-T2 MRI. In: Proceedings of the 25th Annual Scientific Meeting of ISMRM, Honolulu, Hawaii, USA, p. 2668.

Seifert, A.C., Li, C., Wilhelm, M.J., Wehrli, S.L., Wehrli, F.W., 2017. Towards quantification of myelin by solid-state MRI of the lipid matrix protons. Neuroimage 163, 358–367.

Seifert, A.C., Umphlett, M., Hefti, M., Fowkes, M., Xu, J., 2019. Formalin tissue fixation biases myelin-sensitive MRI. Magn. Reson. Med. 82, 1504–1517.

Sheth, V., Shao, H., Chen, J., Vandenberg, S., Corey-Bloom, J., Bydder, G.M., Du, J., 2016. Magnetic resonance imaging of myelin using ultrashort echo time (UTE) pulse sequences: phantom, specimen, volunteer and multiple sclerosis patient studies. Neuroimage 136, 37–44.

Sigalovsky, I.S., Fischl, B., Melcher, J.R., 2006. Mapping an intrinsic MR property of gray matter in auditory cortex of living humans: a possible marker for primary cortex and hemispheric differences. Neuroimage 32, 1524–1537.

Varma, G., Duhamel, G., de Bazelaire, C., Alsop, D.C., 2015. Magnetization transfer from inhomogeneously broadened lines: a potential marker for myelin. Magn. Reson. Med. 73, 614–622.

Waldman, A., Rees, J., Brock, C., Robson, M., Gatehouse, P., Bydder, G., 2003. MRI of the brain with ultra-short echo-time pulse sequences. Neuroradiology 45, 887–892.

Wansapura, J.P., Daniel, B.L., Pauly, J., Butts, K., 2001. Temperature mapping of frozen tissue using eddy current compensated half excitation RF pulses. Magn. Reson. Med. 46, 985–992.

Weiger, M., Pruessmann, K.P., 2019. Short-T2 MRI: principles and recent advances. Prog. Nucl. Magn. Reson. Spectrosc. 114–115, 237–270.

Weiger, M., Brunner, D.O., Dietrich, B.E., Muller, C.F., Pruessmann, K.P., 2013. ZTE imaging in humans. Magn. Reson. Med. 70, 328–332.

Weiger, M., Overweg, J., Rösler, M.B., Froidevaux, R., Hennel, F., Wilm, B.J., Penn, A., Sturzenegger, U., Schuth, W., Mathlener, M., Borgo, M., Börnert, P., Leussler, C., Luechinger, R., Dietrich, B.E., Reber, J., Brunner, D.O., Schmid, T., Vionnet, L., Pruessmann, K.P., 2018. A high-performance gradient insert for rapid and short-T2 imaging at full duty cycle. Magn. Reson. Med. 79, 3256–3266.

Welker, W., 1990. Why does cerebral cortex fissure and fold? In: Jones, E.G., Peters, A. (Eds.), Cerebral Cortex: Comparative Structure and Evolution of Cerebral Cortex, Part II. Springer US, Boston, MA, pp. 3–136.

Wennerström, H., 1973. Proton nuclear magnetic resonance lineshapes in lamellar liquid crystals. Chem. Phys. Lett. 18, 41–44.

Wilhelm, M.J., Ong, H.H., Wehrli, S.L., Li, C., Tsai, P.H., Hackney, D.B., Wehrli, F.W., 2012. Direct magnetic resonance detection of myelin and prospects for quantitative imaging of myelin density. Proc. Natl. Acad. Sci. Unit. States Am. 109, 9605–9610.